Electronic Supplementary Material (ESI) for Soft Matter.

Supplementary Information

Damping the jump of coalescing droplets through substrate compliance

Gopal Chandra Pal[†], Manish Agrawal[‡], Saladi Satya Siddhartha[†], Chander Shekhar Sharma[†]*

[†]Thermofluidics Research Laboratory, [‡]Department of Mechanical Engineering, Indian Institute of Technology Ropar, Rupnagar, Punjab 140 001, India

*Email: chander.sharma@iitrpr.ac.in, Ph: +91-1881-232358

Contents

S1. Experimental setup for microliter droplet coalescence

S2. Image processing for droplet jumping height measurement and error analysis

S3. Fluid-structure interaction model for coalescence-induced droplet jumping on rigid and compliant superhydrophobic substrates

S4. Fast Fourier Transform (FFT) analysis of force exerted by the coalescing droplets on the substrate

S5. Substrate deformation and upward kinetic energy of coalesced droplet

S6. Spring-mass system model for coalescence-induced droplet jumping: derivation of governing equations and model validation

S7. Can coalescence-induced droplet jumping be enhanced by using substrate flexibility?

S8. Effect of droplet size on coalescence dynamics

S9. Experimental details for fog harvesting

S10. List of supplemental videos

S1. Experimental setup for microliter droplet coalescence

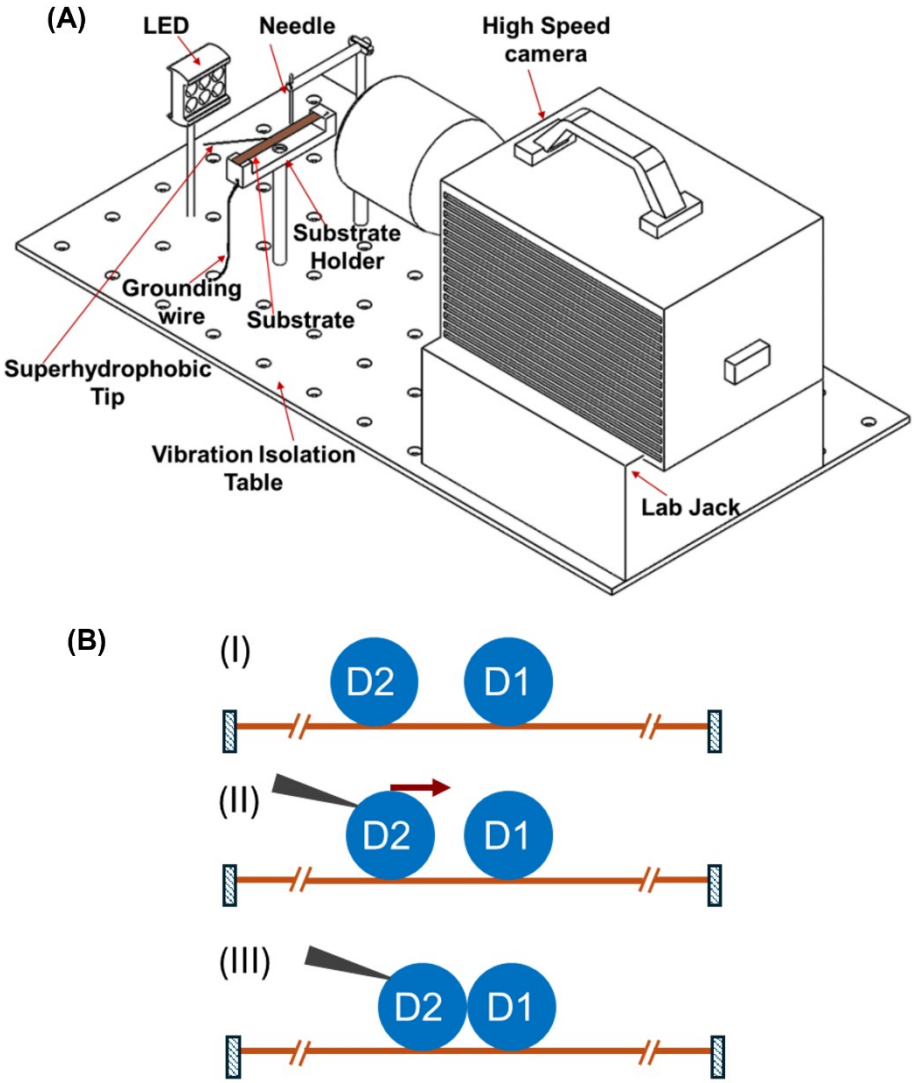

Figure S1: (A)Experimental setup for investigation of coalescence-induced jumping of droplets on rigid and compliant superhydrophobic substrates. **(B)** Droplet position (I) just after dispensing, (II) intermediate stage before coalescence, (III) just before the starting actual coalescence process. The black-colored wedge represents the superhydrophobic wooden tip through which droplet (D2) is pushed slowly towards the other drop (D1).

In each experiment, two droplets of the same size were first carefully dispensed on the substrate using a superhydrophobic micropipette tip, with one droplet, marked as D1 in Figure S1, dispensed at the center of the beam, and the other droplet D2 dispensed at some distance from D1. Subsequently, D2 was slowly moved and brought in contact with D1 using a superhydrophobic wooden tip to trigger coalescence (see Figure S1B). It was ensured that minimal kinetic energy ($\lesssim$ 5% of surface energy of the droplet) was imparted to drop D2 during this movement.

S2. Image processing for droplet jumping height measurement and error analysis

a) Image processing: The images taken by the high-speed camera were processed for measuring the droplet jumping height in both the cases of the rigid and compliant substrate. The compliant substrate deforms by a finite amount $(y_{s,w})$ from the horizontal position due to the self-weight and the weight of the droplets dispensed on it. The substrate deformation due to the force exerted by the coalescence process was measured with respect to this static deformed configuration of the substrate as shown in Fig. S2. We measured $y_{s,w}$ and compared the measurement with theoretical calculation for completeness. The measured static deformation of a copper beam, with length, width and thickness as 40 mm, 4 mm and 20 µm respectively, due to weight of two droplets with D_0 ~1 mm is 46 $\pm$ 13 µm. A simple estimation of beam deflection based on linear stiffness assumption yields a value of ~ 76 µm. A numerical simulation of the beam deflection accounting for the non-linear stiffness yields beam deflection of ~ 57 µm, in close agreement with experiments.

All the experimental images were converted to a binary image through thresholding by using the ImageJ software. After conversion, the droplet motion was analyzed by tracking the movement of the droplet centroid over time. The resulting data was used to estimate the droplet jumping velocity on compliant substrate as $v_{d,jump} \approx \sqrt{2gH_{d,jump}}$ where $H_{d,jump}$ is the vertical distance between droplet centroid position at the moment of jump and at its highest vertical position as shown in Fig. S2. We also estimated $v_{d,jump}$ by fitting a parabolic curve to the droplet trajectory obtained above.[1] Both the estimates yielded similar values of $v_{d,jump}$ with a deviation of less than ~3%. Similarly, we also processed the images to measure the substrate deformation due to the force exerted by the coalescence event.

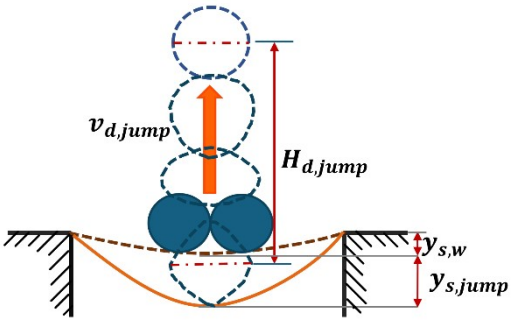

Figure S2: Schematic visualization of substrate deformation, droplet jumping and measurement of $H_{d,jump}$ for estimation of the jumping velocity $v_{d,jump}$.

b) Error analysis:

i) Effect of experimental image processing on droplet movement measurement: When the droplet path as obtained from experimental images is analyzed, a path as shown in inset of Fig. 1(b) in main text is obtained. This undulating path is obtained due to the fact that the droplet centroid location measurement in each image is based on two-dimensional images of the three-dimensional jumping droplet. This aspect contributes towards experimental uncertainty in droplet trajectory which we estimate through multiple repeated trials of each experiment. Another source of uncertainty in centroid location arises from the thresholding of images due to the finite resolution of optical imaging. Hence the net error in centroid location at any time instant is obtained through error propagation as $\Delta E = \sqrt{{\Delta E_s}^2 + {\Delta E_R}^2}$, where ΔE_R is the random error estimated from multiple repeated trials of an experiment and ΔE_s is the systematic error due to finite resolution of image processing.[2]

ii) Effect of droplet dispensing through superhydrophobic micropipette tip: During the coalescence experiments, droplets are dispensed on the substrate using a superhydrophobic tip. We find that there is a variation of less than 4% in terms of droplet diameter in all the repeated trials for particular cases of coalescence on compliant and rigid substrate. We have performed a minimum of three trials for all the cases.

S3. Fluid-structure interaction model for coalescence-induced droplet jumping on rigid and compliant superhydrophobic substrates

a) Calculation of natural frequency, stiffness, equivalent mass and damping coefficient of the compliant substrate: The substrate is modeled as a beam mounted in a fixed-fixed configuration as in the droplet-droplet coalescence experiments. The natural frequency (ω_n) and modal stiffness (k_s) of the substrate is obtained by performing modal analysis in the ANSYS Mechanical software.[3] Here, the governing equation for the modal analysis is given by equation (S1).

$$\left(K - \omega_n^2 M\right)\phi = 0 \qquad \text{(S1)}$$

where K, M and ϕ represent stiffness matrix, mass matrix and mode shape respectively. Grid independence is performed to ensure the correctness of the obtained modal solution. The material properties of copper and aluminum are taken from the substrate manufacturer. For

PDMS, the material properties are obtained from literature.[4] The stiffness (k_s) and natural frequency (ω_n) corresponding to mode 1 for various substrates are listed in Table 1 in main manuscript. The damping ratio for aluminum and copper is taken from the literature and the values were found to be approximately $\sim 10^{-3}$.[5,6] For PDMS substrate, the damping ratio is estimated as $\sim 10^{-2}$ using logarithmic decrement method where $\zeta = (ln|\delta_1/\delta_2)|/2\pi$. $ln|\delta_1/\delta_2)|$ represents the logarithmic decrement.[7] Thus, we have neglected the effect of substrate damping in our analysis.

b) Droplet coalescence on rigid superhydrophobic surface: We adopt 3D Volume-of-Fluid (VoF) method based CFD approach to model the coalescence of sessile droplets on superhydrophobic surface using ANSYS Fluent.[8] We have chosen an incompressible, laminar flow model for our simulation and the contact angle on the surface is assumed to be 180^0. This assumption is valid due to the high advancing contact angle and very low contact angle hysteresis on the fabricated surfaces.[9–11] In this method the following governing equations are solved for mass and momentum conservation of both liquid and gas phase:

$$\frac{\partial \rho}{\partial t} + \nabla \cdot (\rho u) = 0 \qquad \text{(S2a)}$$

$$\frac{\partial (\rho u)}{\partial t} + \nabla \cdot (\rho u \otimes u) = -\nabla p + \mu \nabla^2 u + F_{st} + \rho g \qquad \text{(S2b)}$$

In the above equation, u, p, ρ, μ, and t represents the velocity of mixture, pressure, density, viscosity, and time, respectively. The apparent viscosity μ and density ρ in each cell is calculated by using the following equations:

$$\mu(x,t) = \mu_g + (\mu_l - \mu_g)\alpha \qquad \text{(S3a)}$$

$$\rho(x,t) = \rho_g + (\rho_l - \rho_g)\alpha \qquad \text{(S3b)}$$

Here, ρ_l and ρ_g, μ_l and μ_g are the density and the viscosity of the liquid and gas, respectively. The volume fraction α represents the ratio of cell volume occupied by the liquid to the total volume of the control cell. The numerical value of α in a cell lies between 0 and 1 where $\alpha = 0$ in a cell indicates that the cell is filled with gas while $\alpha = 1$ indicates the cell filled with liquid. Thus α tracks the evolution of the two immiscible phases where the interface between the two phases lies in the cells with α value lying between 0 and 1. The solver solves for the value of α in each cell based on the following transport equation.

$$\frac{\partial \alpha}{\partial t} + u \cdot \nabla \alpha = 0 \tag{S4}$$

The volumetric force F_{st} in equation (S2b) represents the effect of surface tension at the interface. Here, the Continuum Surface Force model[12] is used to capture the surface tension force as a volumetric force as per the following equation:

$$F_{st} = \frac{\gamma_{lv} \rho \kappa \nabla \alpha}{\frac{1}{2}(\rho_l + \rho_g)} \tag{S5}$$

Here the γ and κ represent the interfacial surface tension and the curvature of the interface, respectively. The surface curvature is calculated as $\kappa = -\nabla \cdot (n)$ where $\boldsymbol{n}$ is defined as a unit normal vector given by $n = \left(\frac{\nabla \alpha}{|\nabla \alpha|}\right)$.

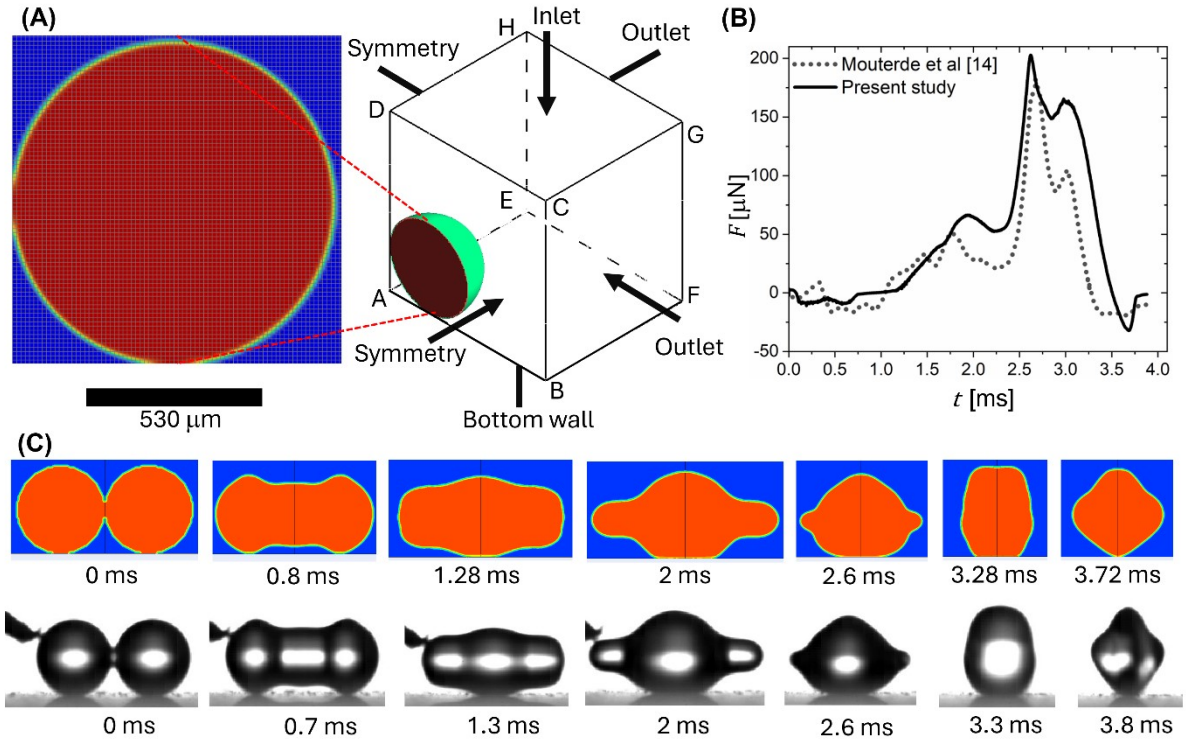

Figure S3: Computational domain details and model validation for coalescence-induced droplet jumping on rigid superhydrophobic surface. **(A)** Computational mesh and boundary conditions for three-dimensional VoF based CFD simulation. **(B)** Transient force validation with literature for a droplet size of 1.06 mm. **(C)** Validation of numerical result (top row) with the experimental result (bottom row) for a droplet size $D_0 =$ 1.06 mm

The computational domain with boundary conditions and the computational mesh is shown in Fig. S3A. The symmetry of the coalescence process is utilized to reduce the overall

computational domain wherein one-half of a coalescing droplet is modeled.[13] This is achieved by imposing symmetry boundary condition on surfaces ABCD and ADEH. No-slip wall boundary conditions and zero velocity inlet boundary condition is imposed on the surfaces ABFE and CDHG, respectively. The surfaces BCGF and EFGH are assigned atmospheric pressure boundary condition. The domain size chosen in our simulation is 4R×4R×4R, where R is droplet radius[13] (see Fig. S3). The grid independence is tested by considering three grids with 26 elements per radius, 40 elements per radius, and 53 elements per radius, respectively for a droplet size of 1 mm diameter. The deviation in force magnitude in the case of 40 and 53 elements per radius is lower than that for the case of 26 elements and 40 elements per radius. Moreover, the maximum force magnitude differs by less than 2.5 % and the droplet detachment time differs by less than 5% for the meshes with 40 and 53 elements per radius. Thus, we have used 40 elements per radius for all the numerical simulations. With the mesh density fixed, the transient force from our numerical model is also validated for a droplet size of 1.06 mm with the literature[14] and shown in Fig. S3B. In addition, the numerical result for the coalescence of droplets with a diameter of 1.06 mm is validated with the corresponding experimental result on a rigid superhydrophobic surface as shown in Fig. S3C.

c) Droplet coalescence on compliant superhydrophobic surface**:** For modeling droplet coalescence on compliant superhydrophobic substrate, in addition to the above described VoF modeling of coalescing sessile droplets, we need to also model the substrate deformation under

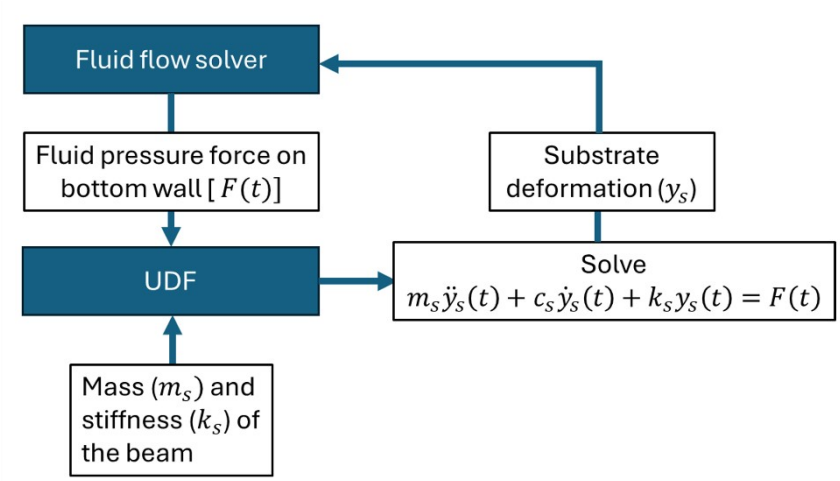

Figure S4: Schematic for fluid-structure interaction model. For every time step, UDF solves Equation 1 from the main manuscript to obtain deformation $y_s(t)$, by taking fluid pressure force $F(t)$ from the fluid flow solver and substrate mass (m_s) and stiffness (k_s) as the input.

the effect of force exerted by coalescing droplets and its effect on the overall coalescence process. For this purpose, we adopt a simplified fluid-structure interaction modeling approach where the substrate deformation is realized through a dynamic moving boundary strategy.[7,15] Here, the bottom wall representing the substrate is set to be a moving boundary, and its motion is defined using a UDF (see Figure S4), based on the substrate deformation calculated by a lumped spring mass system that can account for multiple vibration modes of the substrate.[16] Here, Equation (1)[7,15] from the main text is solved for each mode using the corresponding modal mass, modal stiffness, and modal force to find the contribution of each mode. The force $F(t)$ for this equation at any time t is obtained by integrating the fluid pressure on the wall boundary. The total deformation of the substrate is then obtained by the addition of all these modal contributions. We have taken the assumption of linearity while modeling the substrate as the lumped system. Although the substrate deformation is large relative to substrate thickness, and thus the stiffness is inherently non-linear, we find that the linear lumped spring-mass system model still sufficiently captures the substrate deformation. The lumped mass system is solved using the forward Euler method for every iteration using a user-defined function. The calculated substrate velocity is passed to the solver for the wall motion while the governing equations of mass conservation, momentum and fluid fraction are solved by the pressure solver.[17]

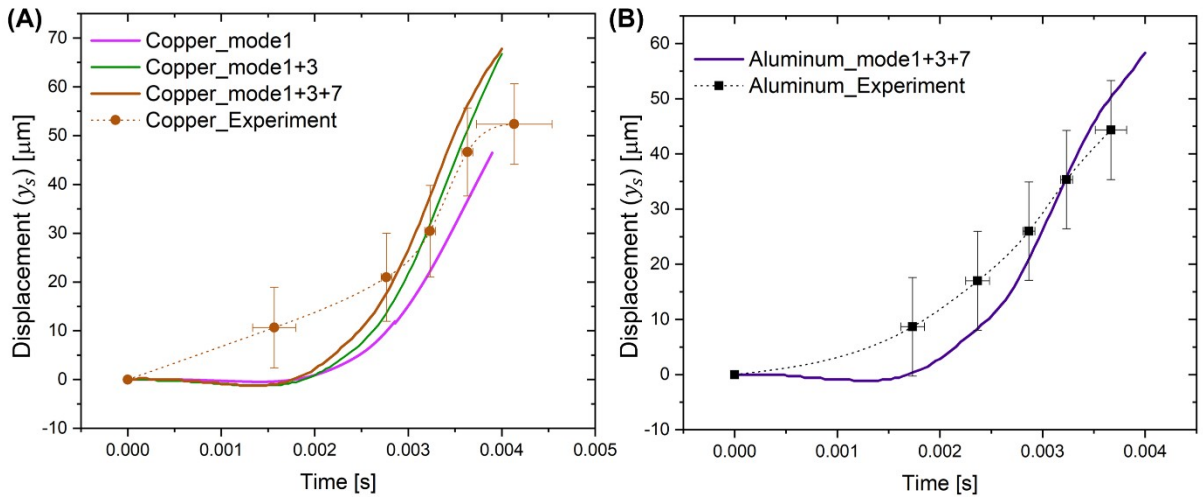

Figure S5: Numerical model validation for compliant substrate. Comparison of substrate displacement obtained from three-dimensional VoF method based simplified fluid-structure interaction modeling framework, by including various number of substrate deformation modes, with the experimental measurements for coalescence of 1.06 mm drops on **(A)** thin Copper substrate and **(B)** Aluminum substrate of 40 mm length.

Modal analysis as discussed in subsection (a) above is used to obtain modal stiffness and modal mass values for multiple modes. This enables us to isolate the dominating modes

for substrate deformation under the force exerted by coalescing droplets, by comparing the predicted substrate deformation against experimental measurements. The experimental substrate deformation values are obtained through high-speed imaging. For instance, Fig. S5A shows the comparison of substrate deformation obtained from experimental measurement and CFD simulations for a thin copper superhydrophobic substrate of 40 mm length (Substrate 4 in Table S1). Three curves are shown for computational results that are obtained by including increasing numbers of substrate vibration modes in the overall calculation. A comparison of predicted and measured substrate deformation shows that accounting for first, third and seventh vibration mode is sufficient for prediction of substrate deformation. This is also validated by the comparison of predicted and measured substrate deformation for another compliant superhydrophobic substrate, a 40 mm long thin Aluminum substrate (Substrate 2 in Table S1), as shown in Fig. S5B. Additionally, we noticed that the first mode accounts for nearly 75% of the substrate deformation in copper and 90% of the substrate deformation for the aluminum case during the droplet coalescence and jumping departure from the substrate. Thus, in order to develop a qualitative understanding of the effect of substrate flexibility parameters on the droplet coalescence process, we considered only the first mode while calculating the substrate deformation in the user defined function and the same modeling approach is adopted for all the computational results shown in Fig. 2b in main text.

S4. Fast Fourier Transform (FFT) analysis of force exerted by the coalescing droplets on the substrate

An FFT analysis has been performed in MATLAB to ascertain the leading harmonic components in the force exerted by coalescing droplets $F(t)$ as obtained from the Fluid-structure interaction model described in section S4. The case of rigid substrate is considered for this analysis. The resulting FFT components for the force applied on the rigid substrate are given in Table S2. We find that the dominating frequency ω_F is within ~15% of droplet oscillating frequency $\left(\omega_d = \frac{2\pi}{\tau_d}\right)$ based on the inertial-capillary time scale for the droplet $\left(\tau_d = \frac{\pi}{4}\sqrt{\frac{\rho D_O^3}{\sigma}}\right)$.[14,16,18] Here, ρ and σ are the liquid density and surface tension respectively.

Frequency ω (rad/s)	A **(μN)**	B **(μN)**
0	0	49.17

1689	-70.86	-19.52
3378	-10.05	-33.60

Table S2: Component of forces from FFT analysis. The first three components, as obtained from FFT analysis, for the force $F(t)$ applied on the rigid superhydrophobic substrate by coalescing droplets with $D_0 = 1\ mm$.

S5. Substrate deformation and upward kinetic energy of coalesced droplet

As two droplets coalesce on a compliant superhydrophobic substrate, the net reduction in surface energy due to coalescence manifests as i) kinetic energy of the coalesced drop and ii) elastic and potential energy of the compliant substrate ii) viscous dissipation. Hence, the energy balance for the overall coalescence process can be expressed as:

$$\sigma \Delta A_{d,jump} = UKE_{d,jump} + IKE_{d,jump} + E_{s,jump} + KE_{s,jump} + E_{d,viscous} \quad \text{(S6a)}$$

Here $\Delta A_{d,jump} = A_{d,0} - A_{d,jump}$ is the net reduction in the total surface area of the two coalescing droplets from initiation of coalescence till the moment of jump t_{jump}. The kinetic energy of the droplet at t_{jump} is the sum of upward kinetic energy $UKE_{d,jump}$ and in-plane kinetic energy $IKE_{d,jump}$. $UKE_{d,jump} = m_d v_d^2(t_{jump})$ where m_d is the mass of each coalescing droplet and $v_d(t_{jump}) = v_{d,jump}$ is the centroidal velocity of the coalesced droplet at t_{jump}. $IKE_{d,jump}$ can be calculated as $IKE_{d,jump} = \frac{1}{2}\int_0^{2m_d} \left(u_{d,jump}^2 + w_{d,jump}^2\right) dm$ where $u_{d,jump}$ and $w_{d,jump}$ are the in-plane (i.e. in x-z plane) local velocities in the coalesced droplet at t_{jump}. Further, the elastic energy stored in the substrate till t_{jump} is $E_{s,jump} = \frac{1}{2} k_s y_{s,jump}^2$ where $y_{s,jump}$ is substrate deformation at t_{jump}. The kinetic energy of the substrate at t_{jump} is $KE_{s,jump} = \frac{1}{2} m_s v_s^2(t_{jump})$ where $v_s(t_{jump})$ is the velocity of the substrate at t_{jump}. Since

viscous dissipation $E_{d,viscous}$ is negligible for the droplets considered in our study,[19] the energy balance can be expressed as:

$$-\sigma\Delta A_{d,jump} = m_d v_{d,jump}^{\ 2} + \frac{1}{2}\rho\int_0^{2V_d}\left(u_{d,jump}^{\ 2} + w_{d,jump}^{\ 2}\right)dV + \frac{1}{2}k_s y_{s,jump}^{\ 2} + \frac{1}{2}m_s v_s^2(t_{jump}) \quad \text{(S6b)}$$

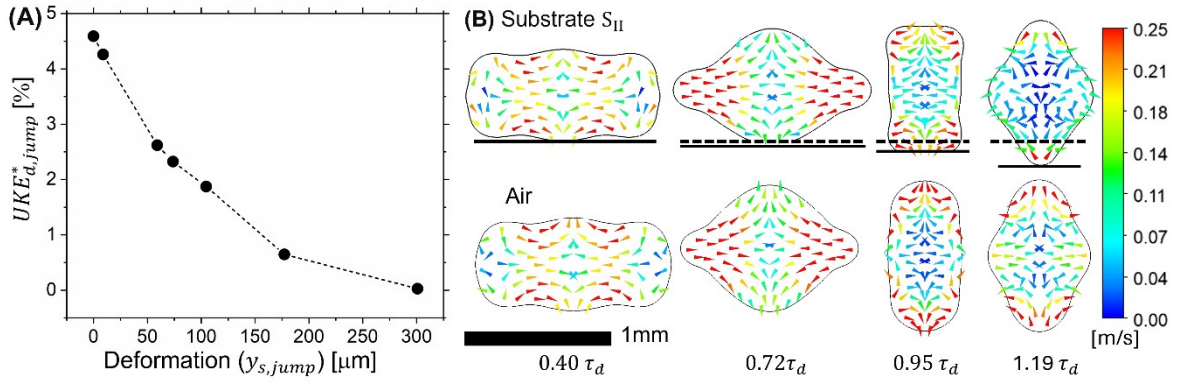

Figure S6: (A) Normalised droplet upward kinetic energy at the moment of droplet jump, $UKE^*_{d,jump} = m_d v_d^2(t_{jump})/(\sigma\Delta A_{d,jump})$ as a function of substrate deformation $y_{d,jump}$. **(B)** Comparison of droplet shape and velocity field evolution for coalescence on substrate S_{II} and in air.

Figure S6A illustrates how droplet upward kinetic energy at the moment of jump reduces with increase in substrate deformation $y_{s,jump}$. Figure S6B compares coalescence process on the substrate S_{II} shown in Fig. 4 and the coalescence process in air. S_{II} accommodates nearly the entire coalescence neck expansion. This minimizes the coalescence asymmetry, and the resulting droplet shape and velocity field evolution for S_{II} closely resembles the case of droplet coalescence in air. This in turn results in a nearly complete suppression of UKE_d during droplet coalescence on S_{II}.

S6. Spring-mass system model for coalescence-induced droplet jumping: derivation of governing equations and model validation

In contrast to spring-mass models for individual droplets bouncing on substrates,[20,21] this spring-mass system model for coalescing droplets as shown in Fig. 5(a) has seven degrees of freedom (DOF). The model can be reduced to a 4-DOF system considering the following aspects of the coalescence process:

a) Since the droplet and substrate always remain in contact from the moment of neck impact till the moment of jump, $y_3(t) = y_2(t)$.

b) Additionally, since the coalesced droplet evolves symmetrically in x-z plane, $x_2(t) = -x_1(t)$ and $z_2(t) = -z_1(t)$.

Thus, the model solves for the coordinates x_1, y_1, y_2 and z_1. The governing equations of motion for this system can be obtained by using the Lagrange formulation. The Lagrangian L for the system can be formulated[16] as:

$$L = \frac{1}{6}m_d\left(2\dot{x}_1^2 + 2\dot{y}_1^2 + 2\dot{y}_1\dot{y}_2 + 2\dot{y}_2^2 + 2\dot{z}_1^2\right) + \frac{1}{2}m_s\dot{y}_2^2 - 2k_d x_1^2 - \frac{1}{2}k_d(y_1 - y_2)^2 - \frac{1}{2}k_s y_2^2 - \lambda(V - V_0) \quad \text{(S7)}$$

The term with Lagrange multiplier λ imposes a volume conservation constraint on the coalesced droplet. The droplet is assumed to be a cuboid with instantaneous volume given by $V = (L_0 + x_1 - x_2)(L_0 + y_1 - y_2)(L_0 + z_1 - z_2) = (L_0 + 2x_1)(L_0 + y_1 - y_2)(L_0 + 2z_1)$, where $L_0 = \sqrt[3]{V_0}$ corresponds to the equilibrium coalesced droplet configuration (a cube with side L_0 with volume equal to a spherical droplet of volume V_0) and $V_0 = \frac{\pi}{3}D_0^3$ is the total volume of two coalescing droplets of diameter D_0.

Since, $\frac{\partial L}{\partial q} - \frac{d}{dt}\left(\frac{\partial L}{\partial \dot{q}}\right) = 0$, where $q = x_1, y_1, y_2, z_1, \lambda$[16], the following governing equations of motion are obtained:

$$\frac{1}{3}m_d\left(2\ddot{y}_1 + \ddot{y}_2\right) + k_d(y_1 - y_2) + \lambda\frac{\partial V}{\partial y_1} = 0 \quad \text{(S8a)}$$

$$\frac{1}{3}m_d\left(\ddot{y}_1 + 2\ddot{y}_2\right) + m_s\ddot{y}_2 - k_d(y_1 - y_2) + k_s y_2 + \lambda\frac{\partial V}{\partial y_2} = 0 \quad \text{(S8b)}$$

$$\frac{2}{3}m_d\ddot{x}_1 + 4k_d x_1 + \lambda\frac{\partial V}{\partial x_1} = 0 \quad \text{(S8c)}$$

$$\frac{2}{3}m_d\ddot{x}_1 + 4k_d z_1 + \lambda\frac{\partial V}{\partial z_1} = 0 \quad \text{(S8d)}$$

$$V - V_0 = 0 \quad \text{(S8e)}$$

The governing equations are converted to non-dimensional form as described below:

$$2\ddot{y}_1^* + \ddot{y}_2^* + k_d^*\left(y_1^* - y_2^*\right) + \lambda^*\frac{\partial V^*}{\partial y_1^*} = 0 \quad \text{(S9a)}$$

$$\ddot{y}_1^* + \left(2 + 3\frac{m_s}{m_d}\right)\ddot{y}_2^* - k_d^*\left(y_1^* - y_2^*\right) + k_d^* y_2^* + \lambda^* \frac{\partial V^*}{\partial y_2^*} = 0 \quad \text{(S9b)}$$

$$2\ddot{x}_1^* + 4k_d^* x_1^* + \lambda^* \frac{\partial V^*}{\partial x_1^*} = 0 \quad \text{(S9c)}$$

$$2\ddot{z}_1^* + 4k_d^* z_1^* + \lambda^* \frac{\partial V^*}{\partial z_1^*} = 0 \quad \text{(S9d)}$$

$$V^* - V_0^* = 0 \quad \text{(S9e)}$$

where

$$x_1^* = \frac{x_1}{D_0},\ y_1^* = \frac{y_1}{D_0},\ y_2^* = \frac{y_2}{D_0},\ z_1^* = \frac{z_1}{D_0},\ V^* = \frac{V}{D_0^3},\ V_0^* = \frac{V_0}{D_0^3} \quad \text{(S10a)}$$

$$t^* = \frac{t}{\tau_d} \quad \text{(S10b)}$$

$$k_d^* = \left(\frac{9\pi}{8}\right)\frac{k_d}{\sigma} \quad \text{(S10c)}$$

$$\lambda^* = \left(\frac{9\pi}{8}\right)\frac{\lambda D_0}{\sigma} \quad \text{(S10d)}$$

The above equations are initialized based on the configuration of the coalesced droplet at the moment of neck impact ($t = 0$ for this model) observed across multiple experimental observations and CFD simulations as shown in Fig. 5(b). The width of the droplet cuboid in x-y plane is taken to be same as that of droplet in this configuration i.e. $L_0 + 2x_1(0) \approx 2D_0$. Further, since the coalescence neck grows equally along y and z direction till it impacts on substrate, $y_1^*(0) - y_2^*(0) = 2z_1^*(0) = 2\xi\ (say)$. Here ξ is obtained based on volume conservation as:

$$\xi = \frac{1}{2}\left(\sqrt{\frac{V_0^*}{\frac{L_0}{D_0} + 2x_1^*(0)}} - \frac{L_0}{D_0}\right) = \frac{1}{2}\left(\sqrt{\frac{V_0^*}{2}} - \frac{L_0}{D_0}\right) \quad \text{(S10)}$$

Thus the initial conditions for the spring-mass system model are specified as:

$$x_1^*(0) = 1 - \frac{L_0}{2D_0} \quad \text{(S11a)}$$

$$y_1^*(0) = 2\xi \quad \text{(S11b)}$$

$$y_2^*(0) = 0 \quad \text{(S11c)}$$

$$z_1^*(0) = \xi \quad \text{(S11d)}$$

$$\dot{x}_1^*(0) = \dot{y}_1^*(0) = \dot{y}_2^*(0) = \dot{z}_1^*(0) = 0 \quad \text{(S11e)}$$

The equations S9 are discretized in time using the forward Euler method. Further, the resulting algebraic non-linear equations are solved with the help of the Newton Raphson method. The moment of jump is defined to be the instant when the total force exerted on the substrate, $F_{tot} = m_s\ddot{y}_2 + k_s y_2 + 2m_d g$, reduces to zero.

The spring-mass system model is able to capture coalescence-induced droplet jumping on compliant substrates as shown in Fig. S7 and Fig. 5(c) of main text. Figure S7 A shows that the predicted substrate deformation and droplet movement show sufficient agreement with

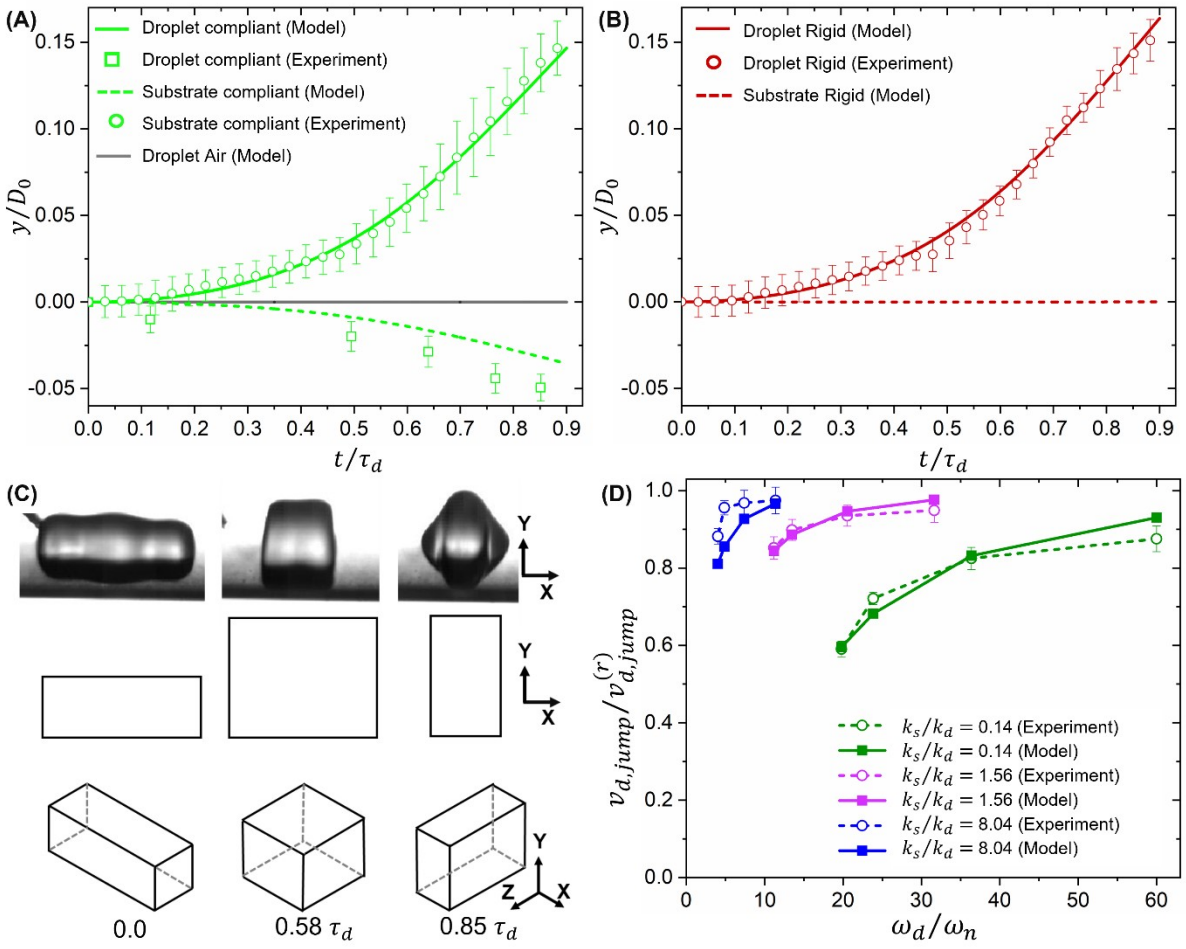

Figure S7: Comparison of spring-mass system model predictions and experimental observations for coalesced droplet trajectory and substrate deformation for coalescence on **(A)** compliant superhydrophobic copper beam and air, **(B)** rigid substrate. Here, $t = 0$ represents the moment of neck impact. **(C)** Comparison of droplet shape from model with the experimental image for coalescence on the compliant superhydrophobic substrate, k=0.01 and $\omega_d/\omega_n = 23.84$. (droplet and substrate trajectory comparison shown in Fig. 5b) **(D)** Effect of k_s and $\frac{\omega_d}{\omega_n}$ on jumping velocity.

experimental data for the case of a compliant superhydrophobic copper beam. The model also correctly captures the two limit cases i.e. droplet coalescence on rigid substrate (high jumping velocity with negligible deformation of the substrate) [Fig. S7 B] and droplet coalescence in air (negligible movement of coalesced droplet centroid) [black curve in Fig. S7 A]. Figure S7 C illustrates the comparison between experimentally observed coalesced droplet shape evolution and the corresponding cuboidal droplet shapes as predicted by the model for coalescence on compliant flexible superhydrophobic substrate (PDMS beam). Further, the model is able to also adequately capture the effect of substrate stiffness and inertia on the coalescence-induced jumping velocity over a wide range of k_s and $\frac{\omega_d}{\omega_n}$ as shown in Fig S7 D.

Further, we have used this model to study the effect of substrate dimensions on coalescence induced droplet jumping. We have considered the coalescence of two 1 mm diameter droplets. For the analysis, we have chosen copper and PDMS material wherein the Young's modulus differs by four orders of magnitude. The droplet jumping velocity for copper

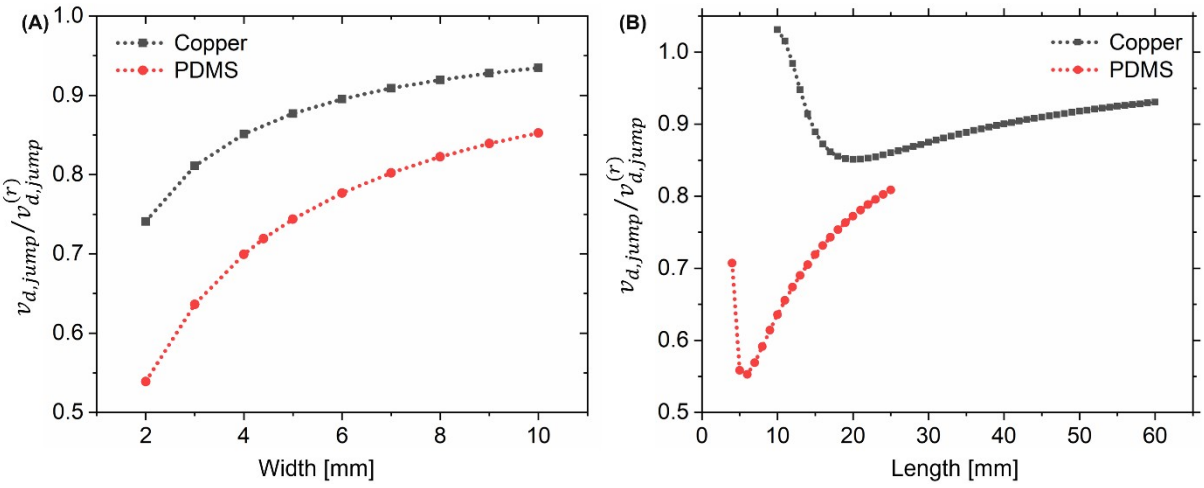

Figure S8: Effect of variation in **(A)** width of copper beam (40 mm length and 10 µm thick) and PDMS beam (15 mm length and 52 mm thick) and **(B)** length of copper beam (4 mm width and 10 µm thick) and PDMS beam (4.4 mm width and 52 mm thick) on jumping velocity for two coalescing droplets of 1 mm diameter.

and PDMS as a function of the beam width and length is shown in figure S8 A and B respectively. In both cases, we have changed either the width or length of the beam by fixing the other dimension. Further, the thickness of the beam is also kept constant. From S8 A, it is evident that the jumping velocity reduces as the beam width is reduced, since a reduction in width translates to a proportional reduction in beam stiffness $(k_s \propto W)$, where W is the beam width, without any change in the beam natural frequency. However, the jumping velocity

shows a non-monotonic trend as a function of beam length in S8 B. As the beam length is increased, the beam stiffness reduces as $(k_s \propto L^{-3})$ while the frequency ratio increases as $\left(\frac{\omega_d}{\omega_n} \propto L^2\right)$, where L is the beam length. Thus an optimum length exists to minimize the droplet jumping velocity in case of both copper and PDMS as shown in the figure. Essentially the beam dimension can be optimized based on the beam material and the size of the coalescing droplets.

S7. Can coalescence-induced droplet jumping be enhanced by using substrate flexibility?

Here, we explore experimentally if it is possible to achieve higher droplet jumping velocity on compliant substrates compared to rigid substrate. As evident from Fig. 3 and Fig. S8D, $\frac{v_{d,jump}}{v_{d,jump}^{(r)}}$ is diminished for substrates with low of k_s and low $\frac{\omega_d}{\omega_n}$ ratio. In all these experiments $\frac{\omega_d}{\omega_n} > 1$. $\frac{v_{jump,c}}{v_{d,jump}^{(r)}} > 1$ can only be achieved if the energy stored in the compliant substrate during neck expansion can be synergistically returned to the coalescing droplets before the jump. This can be feasible only for lower $\frac{\omega_d}{\omega_n}$ ratios.

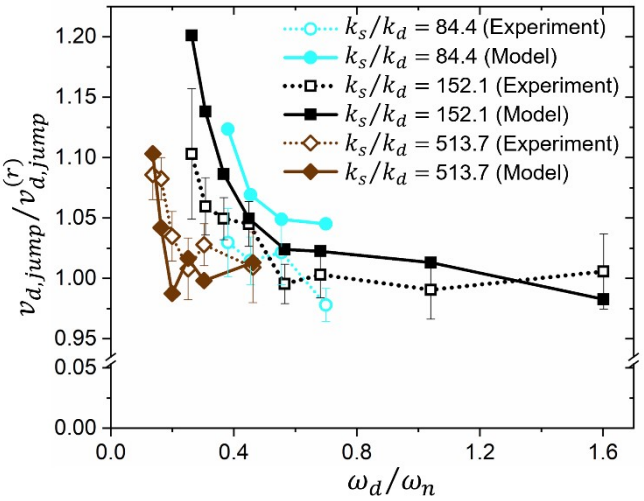

Figure S9: Experimental and predicted variation of $\frac{v_{d,jump}}{v_{d,jump}^{(r)}}$ for multiple substrates with high stiffness.

We perform droplet coalescence experiments on substrates with relatively higher stiffness than the substrates considered earlier and the experimental results are shown in Fig. S8. Here, droplet coalescence experiments are performed on each substrate for a range of D_0. We find that $v_{d,jump}$ does increase beyond $v_{d,jump}^{(r)}$, albeit by only upto ~10%. Further, Fig. S8

also shows that the spring-mass system model is able to sufficiently capture the overall trends in $\frac{v_{d,jump}}{v_{d,jump}^{(r)}}$ for these substrates.

S8. Effect of droplet size on coalescence dynamics

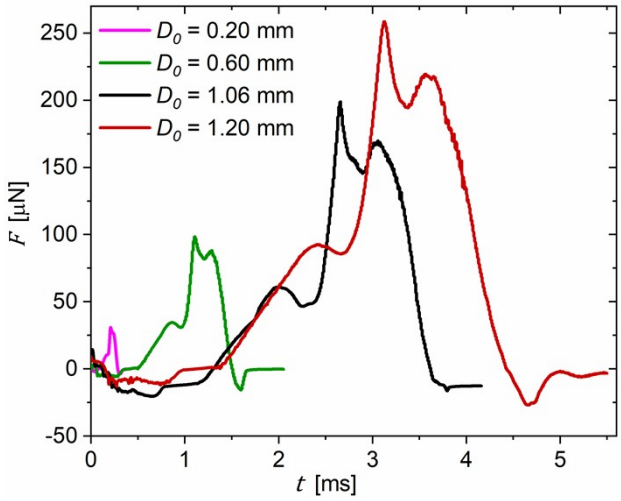

Figure S10: Transient force on substrate due to coalescence-induced droplet jumping. Comparison of force exerted on a rigid superhydrophobic substrate by coalescing sessile droplets for various sizes showing a reduction in magnitude with the reduction in droplet diameter.

Figure S10 shows the force exerted by coalescing drops of various sizes on a rigid substrate. During the coalescence of droplets, surface energy ($\sim\sigma D_0^2$) converts into kinetic energy of the droplet ($\sim\rho D_0^3 U^2$). The characteristic velocity U_d and the characteristic time τ_d scale as $\sim\sqrt{\frac{\sigma}{\rho D_0}}$ and $\sim\sqrt{\frac{\sigma D_0^3}{\gamma}}$ respectively[14]. So, the coalescing force F scales as $\sim\frac{m\times U}{\tau}\sim\sigma D_0$. In addition to the maximum force, the similar nature of force for different sizes of the coalescing droplets indicates that the coalescence dynamics are overall similar across a wide range of droplet sizes.

S9. Experimental details for fog harvesting

In this setup, we have used a copper foil backed by an aluminum plate as the rigid substrate. Two different superhydrophobic compliant substrates are used in vertical cantilever orientation, one made of copper material [Compliant (Copper)] and another from a combination of copper and LDPE material [Compliant (LDPE + copper)] as shown in Fig. S11. The width of the three substrates is set as 13 mm. The substrate length where the fog impinges, L_2, is set as 32 mm for each substrate. While for compliant (copper) substrate, the entire sample is made from a 10 μm thick copper foil, in case of compliant (LDPE + copper) substrate, the L_2 section consists of a 26 μm thick LDPE sheet. For both compliant (copper) and compliant (LDPE + copper) substrates, the total length of the sample L_1+L_2 is 120 mm. Cutouts of 35 mm x 9 mm and 68 mm x 9 mm are made in L_1 section of compliant (copper) and compliant (LDPE + copper) substrate respectively in order to reduce the overall mass and hence increase the natural frequency of substrate (ω_n). The estimated stiffness (k_s) and natural frequency (ω_n) for the compliant (copper) substrate are $\sim 10^{-3}$N/m and ~ 10 rad/s respectively. The corresponding values for compliant (LDPE + copper) substrate are reduced to $\sim 10^{-4}$ N/m and natural frequency $(\omega_n) \sim 8$ rad/s. Thus, while the natural frequency of compliant (LDPE + copper) sample is close to compliant (copper), the stiffness for compliant (LDPE + copper) is about ten times smaller than that for compliant (copper). All the substrates are rendered superhydrophobic by spray coating of Glaco Mirror coat "Zero". (Soft 99 Co.)[14]. The advancing contact angle and contact angle hysteresis for LDPE substrates is 160 ± 1^0 and 3 ± 1^0 respectively, that is nearly identical to wetting properties of the superhydrophobic copper substrate.

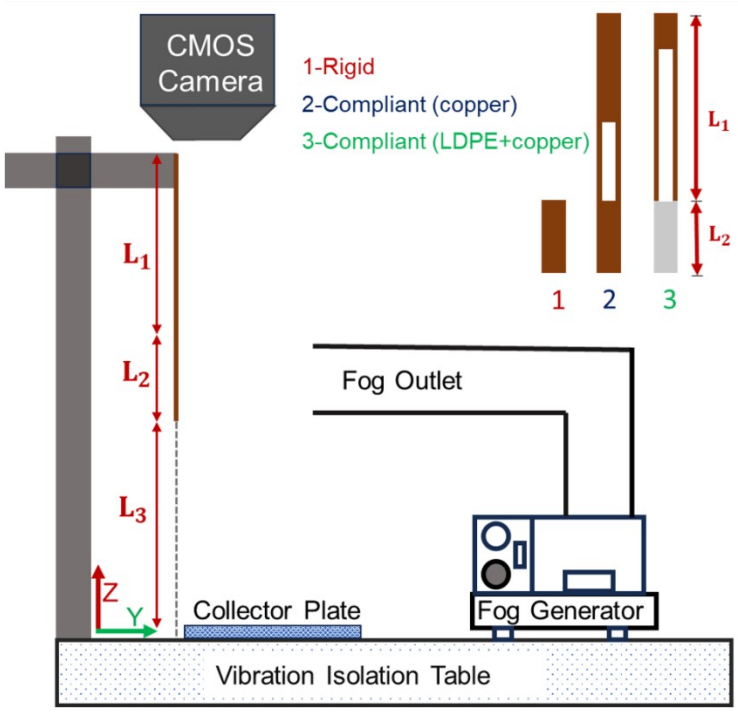

Figure S11: Setup for water collection through fogging on superhydrophobic rigid and compliant surfaces. Inset figure illustrates configuration for the three substrates tested.

A fog generator is used where the generated droplets are of the size of ~6 microns.[22] The distance between fog outlet and substrate is kept the same for a uniform fog density in the case of both rigid and compliant substrates. For each experiment, the sample is suspended at the same distance L_3, above the collector plate. The collector plate is located as shown in Fig. S11 and Fig. 6a of the main paper. The location of the droplets falling on the collector plate is captured through the CMOS camera (Thorlabs Inc.), as shown in Fig. S11. All the experiments are carried out at a similar humidity in the room with a variation of 5-7%.

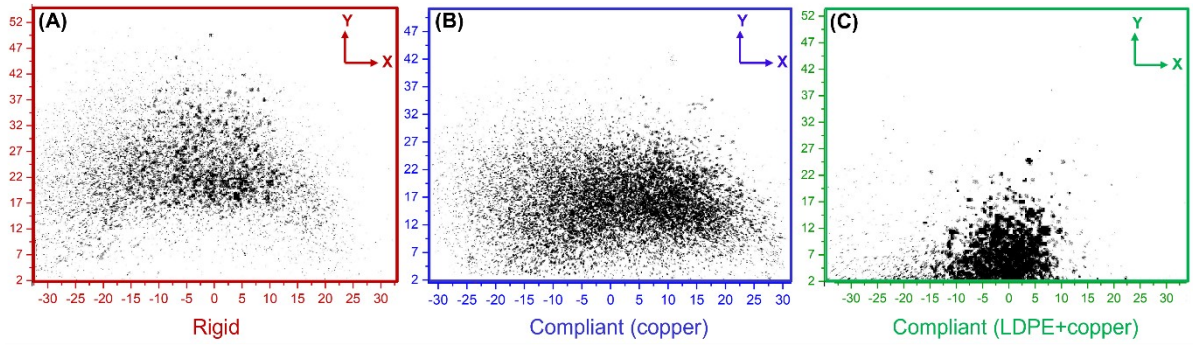

Figure S12: Map of fog water droplets jumping from **(A)** rigid, **(B)** compliant (copper) and **(C)** compliant (LDPE + copper) superhydrophobic surfaces and deposited on a collector plate positioned as shown in Fig. S10. The substrate is 13 mm wide and positioned at x=0 and y=0 (Scale unit is in mm). Figure 6(b) shows a comparison of droplet maps shown above in (A) and (C).

Figure S12 A, B and C show the stacked map of all drops falling from rigid (red), compliant (copper) (blue) and compliant (LDPE + copper) (green) substrate during fog exposure for over 2 hours. In the main manuscript, results are shown only for two extreme cases [rigid and Compliant (LDPE + copper)], substrates. For the case of Compliant (LDPE + copper) substrate the scattering of droplets falling on collector is significantly reduced as compared to the other substrates. Figure S13 shows the comparison of the droplet distributions on the collector plate in terms of normalized area of droplets. Since the droplets deposited on the collector plate are greater than ~100 µm, i.e. much larger than the fog droplets impinging on the substrate, it can be concluded that such droplets depart from the substrate predominantly due to coalescence-induced jumping. The normalized area is calculated by the ratio of total area of droplets on a particular 5 mm strip of the collector plate to the total area of all the droplets fallen on the collector plate. For example, if we take a 5 mm strip between $Y = 7\ and\ Y = 12\ mm$ (point corresponding to 9.5 mm in X axis) for compliant (LDPE+copper) substrate, the total area of droplets on this strip is ~30% of total area of all the droplets deposited on the collector plate. We obtain Fig. 6(c) in the main paper by cumulating the distribution shown in Fig. S13.

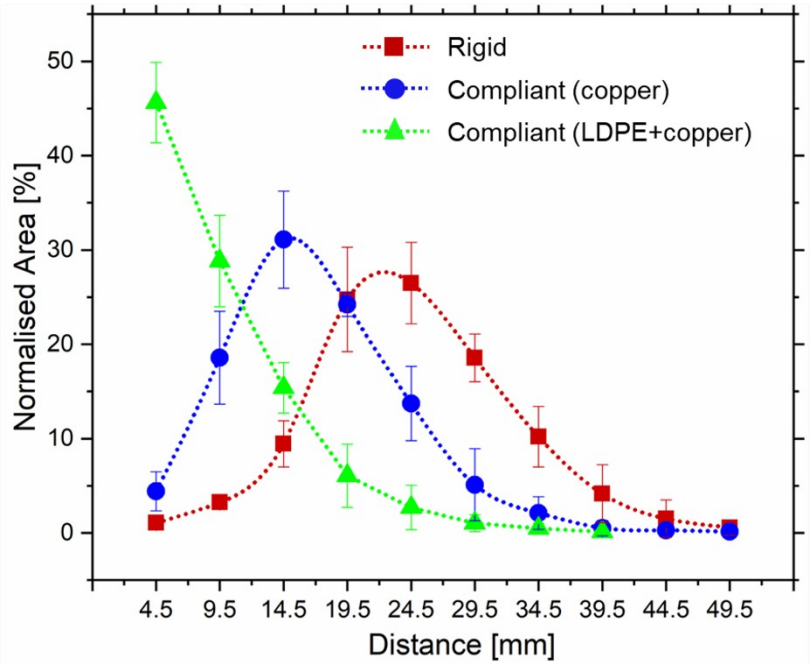

Figure S13: Droplet distribution on the collector plate as a function of distance from the substrate for rigid (Red), compliant (Copper) (blue) and compliant (LDPE + Copper) (green) substrate. The normalized area represents the percentage of total area of the droplet that has fallen on a 5mm strip at a particular distance (shown on x-axis). The number in x-axis represents a particular strip distance, for example distance 4.5mm represents the 5mm strip between 2 -7 mm (along Y direction as shown in Fig. S11).

Next, we utilize the measured droplet distributions on the collector plate to estimate the mean jumping velocity for each substrate. In order to find the mean velocity, we first estimate the underlying probability distribution function (PDF) of the jumping velocities. To find the PDF, we assume that the fog droplets are impinging uniformly over the substrate section L_2. This translates to uniform distribution of jumping droplets over this area. Thus, the PDF for jumping droplet location on the substrate is given by

$$p_Z = \begin{cases} \frac{1}{L_2}, & if\ L_3 \le Z \le L_3 + L_2 \\ 0, & Otherwise \end{cases} \quad \text{(S12)}$$

Further, the droplet distribution on the collector plate is as shown in Fig. S13. In the case of the rigid and compliant (copper) substrate, we approximate the droplet distribution on the collector plate using the Gaussian distribution. The mean of the Gaussian distribution for these substrates is obtained as 27 mm and 16 mm respectively, while the standard deviation is 9 mm and 6.6 mm respectively. In the case of the compliant (LDPE + copper) substrate case, the underlying probability distribution is approximated by the following expression.

$$p_y(y) = ae^{-(by+c)} \quad \text{(S13)}$$

The values of the fitting constants a, b, and c are obtained as 104.8, 101.4, 0.072 respectively.

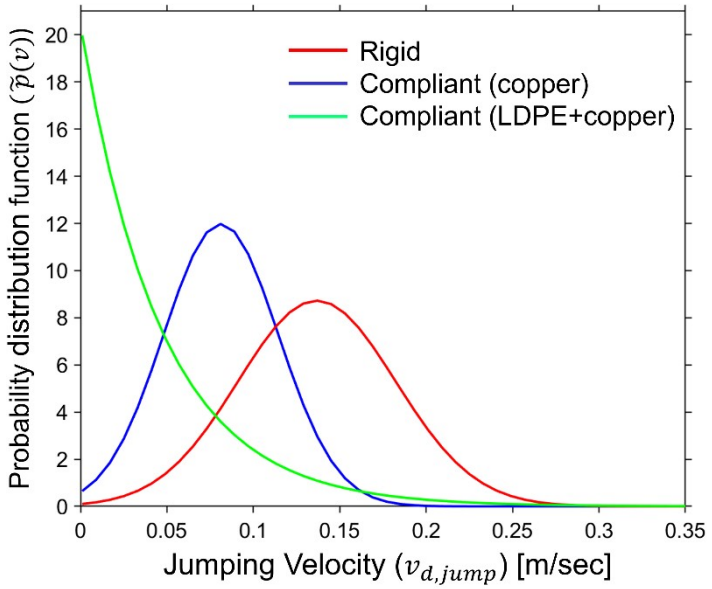

Figure S14: Probability distribution function of jumping velocity for the three substrates.

The PDF of the velocity for the droplet jumping from a fixed location z=z* on the substrate can be expressed as

$$p(v)|_{Z=Z^*} = p_y(Y)\frac{\partial Y}{\partial v} \tag{S14}$$

The overall PDF of the velocity can thus be obtained by integrating the possibility of the various values of location along the z axis.

$$\tilde{p}(v) = \int_0^{L_3+L_2} p(Z^*)p(v)|_{Z=Z^*} dZ^* \tag{S15}$$

The above expression is integrated numerically, and the obtained PDF for droplet jumping velocity for the three samples is shown in Fig. S14. The mean jumping velocities can be obtained from the obtained PDF by the following expression.

$$v_{d,jump} = \int \tilde{p}(v) v \, dv \tag{S16}$$

With the help of the above expression, the jumping velocity ratio $\frac{v_{d,jump}}{v_{d,jump}^{(r)}}$ for the compliant (copper) and compliant (LDPE+ Copper) case is obtained as 0.60 and 0.35 respectively.

S10: List of supplemental videos

Movie S1: Coalescence-induced droplet jumping (~1 mm diameter droplets) on rigid and compliant superhydrophobic substrates. The dashed (red and green) line in the movie represents the initial position of the centroid of coalescing droplets.

Movie S2: Evolution of droplet shape and velocity field for coalescence-induced droplet jumping on rigid and compliant superhydrophobic substrate S_{II} (~1 mm diameter) as obtained from numerical analysis. The solid and dotted horizontal black lines underneath the droplet represent the initial position of the rigid (left) and compliant (right) substrates respectively.

Movie S3: Comparison of coalescence-induced droplet jumping on butterfly wing with and without the rigid support.

Supplementary References:

1 X. Yan, L. Zhang, S. Sett, L. Feng, C. Zhao, Z. Huang, H. Vahabi, A. K. Kota, F. Chen and N. Miljkovic, *ACS Nano*, 2019, **13**, 1309–1323.

2 J. R. Taylor, *An Introduction to Error Analysis*, University Science Books, Sausalito, California, 2nd edn., 1997.

3 *ANSYS Fluent User ' s Guide*, Canonsburg, Technology Drive, 2013, vol. 15317.

4 C. S. Sharma, A. Milionis, A. Naga, C. W. E. Lam, G. Rodriguez, M. F. Del Ponte, V. Negri, H. Raoul, M. D'Acunzi, H. J. Butt, D. Vollmer and D. Poulikakos, *Adv. Funct. Mater.*, 2021, **32**, 11.

5 H. Mevada and D. Patel, *Procedia Eng.*, 2016, **144**, 110–115.

6 L. Cremer, M. Heckl and B. A. T. Petersson, *Structure-Borne Sound Structural Vibrations and Sound Radiation at Audio Frequencies 3 rd edition*, 2005, vol. 1.

7 J. H. Kim, J. P. Rothstein and J. K. Shang, *Phys. Fluids*, 2018, **30**, 9.

8 Inc. ANSYS, *ANSYS Fluent Theory Manual 2021 R2*, Canonsburg,PA, 2021 R2., 2021.

9 M. Reyssat, D. Richard, C. Clanet and D. Quéré, *Faraday Discuss.*, 2010, **146**, 19–33.

10 H. Vahabi, W. Wang, J. M. Mabry and A. K. Kota, *Sci. Adv.*, 2018, **4**, eaau3488.

11 F. Liu, G. Ghigliotti, J. J. Feng and C. H. Chen, *J. Fluid Mech.*, 2014, **752**, 39–65.

12 J. U. Brackbill, D. B. Kothe and C. Zemach, *J. Comput. Phys.*, 1992, **100**, 335–354.

13 H. Vahabi, W. Wang, S. Davies, J. M. Mabry and A. K. Kota, *ACS Appl. Mater. Interfaces*, 2017, **9**, 29328–29336.

14 T. Mouterde, T. V. Nguyen, H. Takahashi, C. Clanet, I. Shimoyama and D. Quéré, *Phys. Rev. Fluids*, 2017, **2**, 1–7.

15 C. Zhang, Z. Wu, C. Shen, Y. Zheng, L. Yang, Y. Liu and L. Ren, *5020 | Soft Matter*, 2020, **16**, 5020.

16 W. T. Thomson, *Theory of Vibration with Applications*, CRC Press, 2018th edn.

17 X. Zhang, M. Hu, J. Cai, A. Babenko, E. Shiju and Z. Xu, *Shock Vib.*, 2022, **2022**, 13.

18 T. Vasileiou, J. Gerber, J. Prautzsch, T. M. Schutzius and D. Poulikakos, *Proc. Natl. Acad. Sci.*, 2016, **113**, 13307–13312.

19 X. Yan, L. Zhang, S. Sett, L. Feng, C. Zhao, Z. Huang, H. Vahabi, A. K. Kota, F. Chen and N. Miljkovic, *ACS Nano*, 2019, **13**, 1309–1323.

20 T. M. Schutzius, S. Jung, T. Maitra, G. Graeber, M. Köhme and D. Poulikakos, *Nat. 2015 5277576*, 2015, **527**, 82–85.

21 G. Graeber, K. Regulagadda, P. Hodel, C. Küttel, D. Landolf, T. M. Schutzius and D. Poulikakos, *Nat. Commun.*, 2021, **12**, 1–7.

22 *Air Compressing Nebulizer 405A/B User's manual*, yuwell, P.R. China.